Carbon Trends 18 (2025) 100436

Contents lists available at ScienceDirect

Carbon Trends

journal homepage: www.elsevier.com/locate/cartre

Enhancing specific capacitance and energy density in printed supercapacitors: The role of activated wood carbon and electrolyte dynamics

Hamed Pourkheirollah [a,*], Remuel Isaac M. Vitto [a], Aleksandrs Volperts [b], Steffen Thrane Vindt [c], Līga Grīnberga [d], Gints Kučinskis [d], Jari Keskinen [a], Matti Mäntysalo [a]

[a] Faculty of Information Technology and Communication Sciences, Tampere University, Tampere, Finland
[b] Latvian State Institute of Wood Chemistry, Riga, Latvia
[c] InnoCell ApS, Svendborg, Denmark
[d] Institute of Solid-State Physics, University of Latvia, Riga, Latvia

ARTICLE INFO

Keywords:
Printed supercapacitors
Energy storage
Activated wood carbon
Energy density
Specific capacitance
Graphitization

ABSTRACT

This study investigates Activated Wood Carbon (AWC) as an electrode material for advancing printed supercapacitors (SCs). AWC, derived from biomass, offers a sustainable alternative to conventional activated carbons. The research highlights the interplay between AWC's structural properties and electrolyte compatibility, addressing challenges in energy storage technologies. Comprehensive analyses, including sorptometry, Raman spectroscopy, X-ray diffraction (XRD), and electrochemical assessments, reveal that AWC's graphitization and structural ordering significantly influence its performance.

Printed SCs fabricated with AWC demonstrate superior performance compared to those using benchmark Kuraray YP-80F activated carbon, achieving up to 93 % and 90 % higher specific capacitance and energy density at 1.0 V and 1.2 V, respectively. The enhanced performance is attributed to AWC's increased surface area and pore volume, which provide abundant ion storage sites and improve ion mobility. Furthermore, the porous structure of AWC facilitates better compatibility with $K_xH_yPO_4$ electrolytes compared to NaCl, with pseudocapacitive effects also contributing to the improved energy storage behavior.

This work underscores the potential of biomass-derived carbon materials in creating high-performance, sustainable SCs. Future efforts will focus on optimizing electrode and electrolyte configurations to further enhance device performance, supporting the transition toward renewable energy solutions.

1. Introduction

Depletion of non-renewable fossil resources and subsequent increases in greenhouse gas emissions have increased the importance of switching to sustainable energy sources such as solar [1], hydro [2], and wind [3]. The transition to sustainable energy sources is vital in order to reduce environmental pollution caused by the widespread use of fossil fuels as well as to address the escalating threat of climate change. Because renewable energy sources are intermittent, they present challenges for meeting the growing energy demand, underscoring the need for effective energy harvesting and storage solutions. This reinforces the transition to sustainable energy [4]. During this transition, energy storage devices play an important role, since they allow the systems to store energy and access it when required, particularly in the absence of a primary power source [5]. As a result, there has been a surge in research aimed at developing high-energy and high-power electrochemical energy storage systems to meet the rising demand for efficient energy production and storage. Among these storage solutions, batteries and supercapacitors (SCs) stand out as prominent components of energy storage systems.

SCs have gained significant attention as energy storage devices in Internet of Things (IoT) devices [6], Artificial Intelligence (AI) applications [7], and various low-power uses like energy-autonomous wearable electronics [8] and self-powered wireless sensor networks [9]. SCs can be classified into Electrochemical Double-Layer Capacitors (EDLCs), which store energy via electrostatic adsorption between ions

* Corresponding author.
E-mail address: hamed.pourkheirollah@tuni.fi (H. Pourkheirollah).

https://doi.org/10.1016/j.cartre.2024.100436
Received 26 November 2024; Accepted 7 December 2024
Available online 8 December 2024
2667-0569/© 2024 The Author(s). Published by Elsevier Ltd. This is an open access article under the CC BY license (http://creativecommons.org/licenses/by/4.0/).

and electrode surfaces relying on a physical charge storage mechanism forming an electrical double layer at electrode-electrolyte interfaces, and pseudocapacitors, which utilize fast and reversible redox reactions at electrode surface during charging and discharging [10].

The widespread adoption of SCs can be attributed to their impressive performance characteristics, such as rapid charge propagation rates and superior capacitance retention [11]. Furthermore, SCs have several advantages over batteries. This includes low equivalent series resistance (ESR), which enables efficient energy transfer, ultra-high power density, which facilitates rapid energy delivery, and long cycle life, which allows repeated charging and discharging cycles with little degradation [12,13,14]. Additionally, SCs provide quick charging and discharging capabilities without the risk of undercharging, as with many batteries, but they still require proper charge termination in order to avoid overcharging [15]. Moreover, they are also highly efficient in terms of coulombic efficiency, as well as stable and reliable [16,17]. Despite these strengths, SCs are not without limitations. In general, they have a lower energy density than most batteries, which makes them less suitable for applications requiring large amounts of energy storage [18]. A secondary disadvantage of SCs is that they tend to have higher self-discharge rates and a higher cost per watt-hour (Wh) [19].

Combining advanced materials science with sustainable practices is key to unlocking the full potential of energy storage technologies, paving the way for a more sustainable and efficient future [20]. The performance of SCs can be optimized and enhanced by the use of advanced electrode materials. Industrial demand for cost-effective and high-performance electrode materials necessitates the use of sustainable materials. Various morphologies of porous carbon-based materials have been explored in pursuit of superior and sustainable electrode materials including activated carbons (ACs), carbon fibers, graphene, carbon nanotubes (CNTs), carbon nanoparticles, and carbon aerogels [21–27]. The advantages of these materials include their large surface area, significant and adaptable porosity, increased power density, enhanced conductivity, stability in chemical composition, cost-effectiveness, abundant natural presence, and environmental compatibility [21,22,26]. As a result of its many advantages, including its tunable properties, ample electrolyte pathways, affordable pricing, abundant surface area, and ease of manufacture, AC dominates the market for commercial SC electrodes [21,28]. Although carbon-based materials, including AC, typically exhibit a low energy density, there is still room for improvement in order to meet the commercialization criteria for SCs. As a result, much effort has been devoted to improving the charge storage process in carbon-based materials by refining their structure, morphology, and composition.

Biomass, recognized for its green and renewable nature, emerges as a promising carbon source for AC synthesis [29]. Ongoing research endeavors prioritize the optimization of surface area and specific capacity. Additionally, the integration of renewability, biodegradability, and nontoxic features into AC production from biomass waste not only presents a sustainable solution but also opens up economic avenues. On the other hand, the ease in achieving high surface area with well-defined adjustable pores further enhances the appeal of environmentally friendly approaches in materials science. A variety of biomass carbon sources, including waste coffee beans [30], nutshells [31], animal bone [32], waste newspaper [33], wood and its waste [34], bamboo [35], cotton [36], sugarcane bagasse [37], flowers [38], rice husks [39], corncob [40], and tea leaves [41] have been utilized in the development of electrode materials for SCs.

In addition to the materials themselves, the lightweight nature of the electrode, as well as its high loading, rapid ion diffusion, and excellent conductivity, play an important role in electrochemical energy storage [42]. The carbonized wood (CW) electrode benefits from carbon materials in that it is lightweight, has a large surface area, has excellent electrical conductivity, and is chemically resistant [43]. Furthermore, as a result of policies to increase the use of wood due to its carbon storage properties and adaptability to climate change, there is an expectation that significant quantities of wood waste will enter the waste stream over the next fifty years [44]. As a result of this phenomenon, sustainable practices in material utilization are becoming increasingly important. As a result, microscopic channels found within the CW electrode, which are a result of its cellular structure, are able to streamline the paths of ion diffusion and reduce resistance [45]. In addition to allowing for greater loading of active materials, this feature enhances the overall energy density of the device significantly.

Recently, various methods have been reported for utilizing wood biomass to produce AC for use as electrode materials in SCs. A novel and cost-effective method for creating hierarchical porous ACs from acacia wood has been developed by Hamouda et al. [46]. By using activating agents such as KOH, $ZnCl_2$, and H_3PO_4, they were able to produce different types of ACs, including AWC-K, AWC-Z, and AWC-P. AWC-K demonstrated exceptional properties as an SC electrode, including a large specific surface area of 1563.43 m2/g and a high specific capacitance of 224.92 F/g. The AWC-K//AWC-K symmetrical SC device exhibited a high energy density of 23.98 Wh/kg as well as excellent cycling stability. Acacia wood-based ACs can enhance energy storage applications with this innovative approach. In another study, Selvaraj et al. synthesized AC via KOH activation-carbonization using birchwood popsicle sticks [47]. As a result of the KOH activation, the pore distribution was altered, enhancing the specific surface area. As the activation temperature was increased to 800 °C, abundant micro- and mesopores were produced, resulting in a greater surface area and pore volume. Furthermore, physical properties and electrochemical characteristics were examined, including specific capacitance and impedance characteristics. Separately, Atika et al. developed oxygen-functionalized porous activated carbon from eucalyptus wood for SC electrodes using KOH activation at 600 °C [48]. A comparison was made between its specific capacitance and that of PACE activated at 800 °C. PACE was activated with KOH to get a high specific surface area with micro- and mesopores and incorporate oxygen functionality. According to Chen et al. [49], by using a low inert gas flow rate during carbonization, active gases (CO2 and water vapor) were retained, which enabled self-activation of CW electrodes. Their study examined the effects of pre-oxidation temperature, carbonization temperature, and gas flow rate on self-activation and demonstrated high energy densities and stability in wood-structured symmetric SCs. In another publication, Jain et al. described using a mixture of European deciduous trees – Birch, Fagaceae, and Carpinus betulus – to create biomass-derived porous carbon [50]. An electrode material for EDLCs was made from this carbon. In contrast to existing methods requiring higher temperatures and longer times, their approach involved pyrolysis at 500–700 °C for 10 min, a simpler process. Cavitation in acidic conditions assisted in activating, removing impurities, and generating porosity. European deciduous trees were chosen due to their heteroatom richness, which enhances the formation of pores during high-temperature pyrolysis.

The study outlined in this work encompasses the synthesis of four distinct carbon materials, derived from alder wood charcoals, of variable size and type through a thermal carbonization process facilitated by LSIWC (project partner). These materials were subsequently refined to achieve uniform particle size distribution. A key novelty of this study is the use of sodium hydroxide (NaOH) as the activation agent during the carbonization process. This approach is notably less common than the conventional use of potassium hydroxide (KOH), providing a fresh perspective on activation methodologies for biomass-derived carbons. Furthermore, sorptometry results for AWC samples reveal a significantly higher BET surface area and micropore area compared to the commercial benchmark Kuraray YP-80F, demonstrating the superior structural properties achieved in this work.

Our approach to developing ACs for electrode materials involved iterative refinement based on structural, morphological, and electrochemical analysis, with optimization aimed at maximizing graphene content. Finally, printed SCs fabricated with inks derived from these four AWC materials exhibited significantly enhanced specific capacitance as

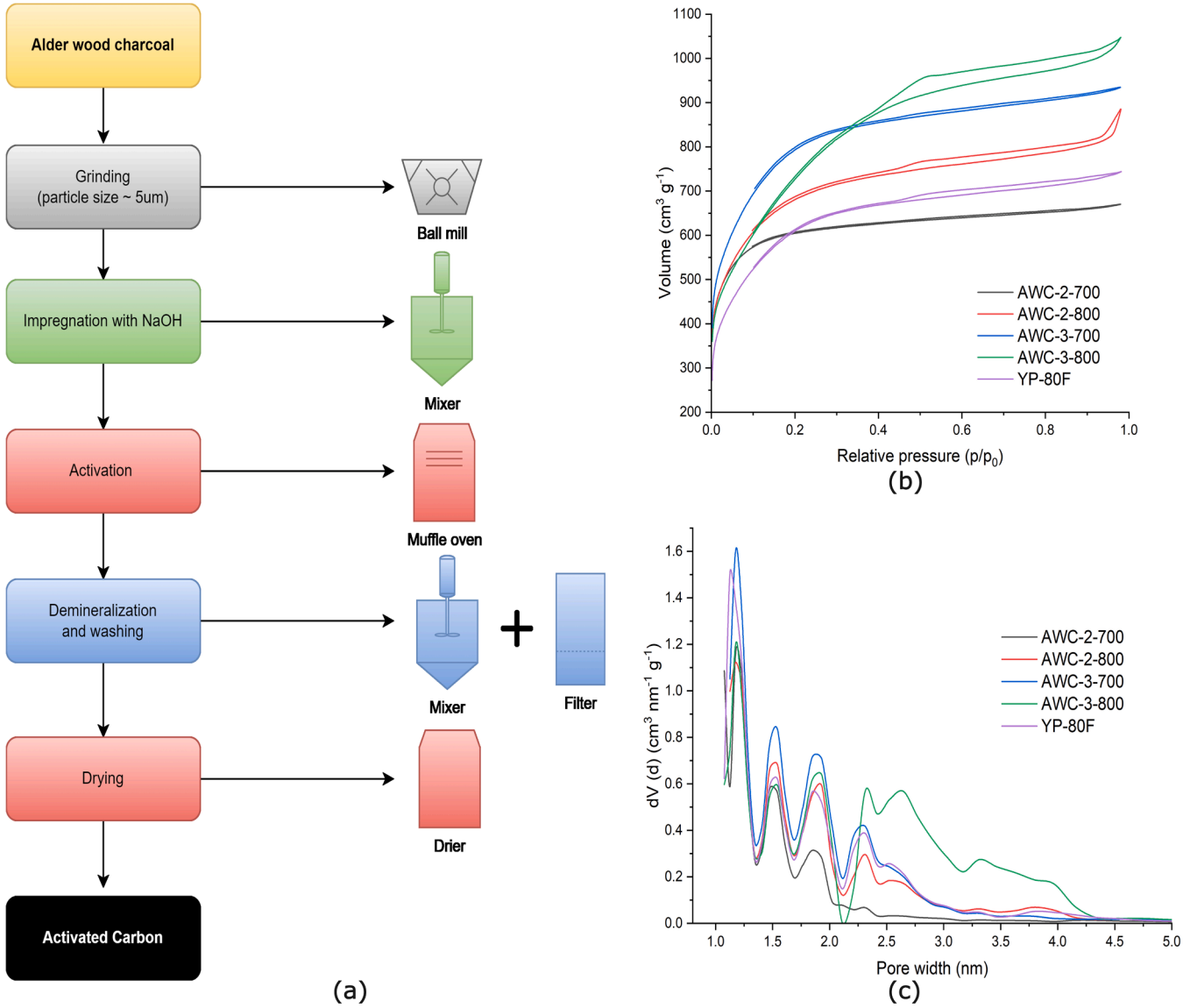

Fig. 1. (a) Schematic representation of AWC materials' activation process. (b) Microporous structure evident in nitrogen sorption isotherms at 77K. (c) DFT analysis reveals mesoporosity variations influenced by temperature and NaOH addition.

well as energy density compared to commercial counterparts, underscoring the efficacy of our approach. Furthermore, two aqueous electrolytes, NaCl and KxHyPO4, were selected for this work because of their environmental friendliness and distinct advantages over widely used alternatives such as KOH and Na_2SO_4. $K_xH_yPO_4$ was chosen for its high buffer capacity, which enhances stability during operation [51], and its substitution of the highly corrosive KOH allows for safer and more straightforward experimentation. NaCl was selected due to its wide availability and the ability to achieve lower operating temperatures compared to Na_2SO_4, whose solubility rapidly decreases at lower temperatures. While Na_2SO_4 might offer better electrochemical stability of the anion in most cases, NaCl provides practical benefits for this study, including ease of handling and compatibility with the AWC materials. These choices align with the study's focus on environmentally friendly and practical solutions for advancing supercapacitor technology.

2. Experimental

2.1. Electrode materials

The electrode materials utilized for the printed SCs comprise four variants of AWC (Activated Wood Carbon) materials manufactured by LSIWC, alongside the commercially available Kuraray YP-80F for comparison. The activation process for the AWC materials is detailed as follows.

Alder wood charcoal was processed to enhance its porosity and surface area. Initially, the charcoal underwent a two-step grinding process using a cutting mill (Retsch SM-100) and a Fritsch planetary mill Pulverisette 5/2 equipped with zirconia mortars and balls, resulting in particles approximately 5 μm in size. Subsequently, the ground charcoal was impregnated with NaOH in ratios ranging from 2 to 3 gs of alkali per gram of carbonaceous precursor.

The impregnated charcoal was then thermochemically activated in a Nabertherm 40 L muffle oven under argon atmosphere at temperatures of 700 °C and 800 °C for 1 hour. This process facilitated the removal of volatile components and reactions with surface functionalities, creating a high number of randomly distributed slit-like pores in the carbonized raw material and thus resulting in a highly porous material. Post-activation, the samples underwent demineralization by boiling in 10 % HCl for 2 h, followed by washing with deionized water until a neutral pH was reached.

Fig. 1a illustrates the sequential steps involved in the process, which

Table 1
Sorptometry data summary of AC materials.

	Unit	AWC 2–700	AWC 2–800	AWC 3–700	AWC 3–800	YP-80F
MultiPoint BET surface area	m^2/g	2099	2431	2866	2669	2220
DR method micropore area	m^2/g	2377	2356	2772	2328	2063
DFT cumulative surface area	m^2/g	1696	1744	1923	1754	1352
DR method micropore volume	cc/g	0.8449	0.8373	0.9852	0.8257	0.7333
DFT cumulative pore volume	cc/g	0.9258	1.206	1.302	1.465	1.036
Average pore diameter	nm	1.976	2.251	2.017	2.428	2.074
DR method micropore pore width	nm	1.348	1.332	1.498	1.377	1.521

include grinding, impregnation with NaOH, thermal activation, demineralization, and drying. A systematic approach has been developed for preparing AC from alder wood charcoal in order to customize its properties for specific applications.

Comprehensive volumetric and surface area sorptometry analyses, including surface area metrics, pore volume data, and pore size distribution, are presented in Table 1 for each AC material utilizing a diverse array of methodologies such as MultiPoint BET (Brunauer-Emmett-Teller), DR (Dubinin-Radushkevich) method, and DFT (Density Functional Theory) method. The sorptometry analyses were conducted utilizing 'Quantachrome NOVA 4200K' instrumentation. For a deeper understanding of these analysis techniques, please refer to [52,53].

Analysis of nitrogen sorption isotherms at 77 K (depicted in Fig. 1b) reveals that all samples exhibit a developed microporous structure. Additionally, variations in activation temperature and/or NaOH addition rate result in the emergence of hysteresis loops in the isotherms, indicating capillary condensation and the evolution of mesoporosity. Notably, the sample synthesized at 800 °C with a NaOH ratio of 3 (AWC-3–800) demonstrates the highest degree of mesoporosity, while the one prepared at 700 °C with a ratio of 2 (AWC-2–700) exhibits the least, as evidenced by pore size distribution analysis conducted via DFT (as shown in Fig. 1c).

According to Table 1, the sorptometry measurements revealed distinct characteristics among the investigated AWC samples. From AWC-2–700 to AWC-3–700, the BET surface area measurements revealed a general increase, with AWC-3–700 showing the highest surface area, followed by a slight decrease for AWC-3–800. As a result of this pattern, it appears that carbonization at 700 °C is ideal for increasing surface area, especially when a higher precursor ratio is used, such as in AWC-3–700. Compared to Kuraray YP-80F, all experimental samples demonstrated higher surface areas, indicating that the activation process used for these samples was more effective than that used for Kuraray YP-80F.

Both the DR method and DFT measurements indicate that AWC-3–700 has the highest pore volume, emphasizing its superior adsorptive properties. While increasing temperatures generally promote pore development by enhancing the activation process and facilitating the removal of volatile components, there appears to be a diminishing return or even a slight reduction in pore volume beyond a certain temperature threshold, as observed with AWC-3–800. This effect can be explained by the potential collapse or shrinkage of pores at higher temperatures, which may occur due to the formation of more rigid and dense carbon structures. At elevated temperatures, the carbon framework can undergo further densification or graphitization, leading to a reduction in the number of accessible pores. This balance between activation and pore preservation is likely why AWC-3–700 demonstrates

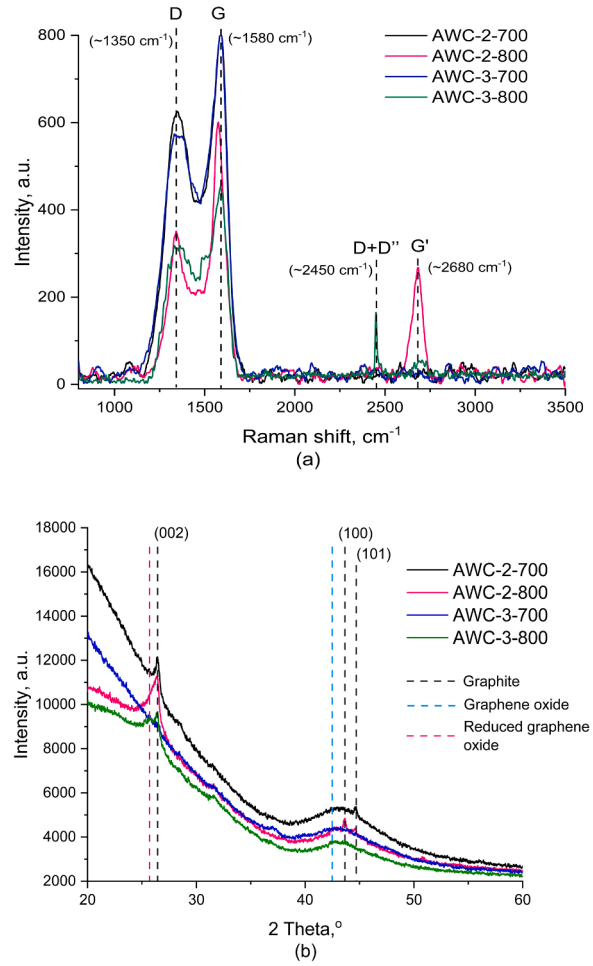

Fig. 2. (a) Raman spectroscopy and, (b) XRD analysis of four AWC samples.

superior performance, with optimal pore development and preservation compared to AWC-3–800.

Analysis of the pore size distribution revealed that the average pore diameter increased from AWC-2–700 to AWC-3–800, suggesting that higher temperatures may promote the formation of larger mesopores and macropores. In various adsorption processes, which require pores of different sizes for optimal performance, this range in pore sizes is advantageous.

Additionally, Fig. 2 displays RAMAN (TriVista CRS Confocal TR777, Spectroscopy & Imaging GmbH, Germany) as well as X-ray diffraction (XRD) (MiniFlex600, Rigaku Corporation, Japan) analyses for each AWC sample. AWC samples can be characterized by Raman spectroscopy to gain insight into the molecular arrangements and structural characteristics associated with them. It is evident from the Raman spectra that the carbonaceous structure varies at different wavenumbers, as indicated by the differential peak intensities. In addition, Raman spectroscopy analysis results confirmed the sorptometry analysis findings by showing a trend in the graphitization process. Accordingly, the peak intensities across the spectrum of AWC-2–800 indicate the highest level of graphitization or structural order compared to the other samples, thereby contributing to mechanical stability and conductivity. Furthermore, the observed trends in peak intensities provide insights into the relative crystallinity and graphitic nature of the investigated AWC samples. As the graphitization trend decreases from AWC-2–800 to AWC-3–800, AWC-2–700, and AWC-3–700, this indicates that not all processing conditions favor the formation of ordered structures of carbon. Besides, Raman spectroscopy confirmed the presence of 2-dimentional graphene-like structures in the synthesized carbons, as evidenced by the

Table 2
Raman analysis results showing ID/IG ratios and FWHM of the G peak.

Sample	ID/IG	FWHM (G) (cm^{-1})
AWC-2–700	2.31	108.72
AWC-3–700	2.43	108.99
AWC-2–800	1.86	91.83
AWC-3–800	3.18	93.83

appearance of the G' peak.

The deconvolution of the Raman peaks was performed to determine the D/G peak intensity ratio. The Origin software was used for the initial signal processing, baseline subtraction, and Gaussian functions were applied for peak fitting. The ID/IG ratios, along with the full width at half maximum (FWHM) of the G peak, were calculated for each sample and are presented in Table 2. Results shows that sample AWC-3–800 has the most defects and is more disordered (amorphous) compared to sample AWC-2–800, which has a lower ID/IG ratio, therefore higher crystallinity rate.

Lastly, XRD analysis further elucidates the structural properties of the AWC samples. The XRD patterns exhibit characteristic diffraction peaks corresponding to the crystalline phases present in the samples. XRD analysis revealed that AWC-2–800 displays the highest intensity peaks, indicating a greater degree of crystallization compared to the other AWC samples. In all samples, the XRD pattern exhibits a broad peak at around 43.3°, corresponding to the diffraction of (1 0 0/1 0 1) planes in the disordered amorphous structure. Additionally, a sharper peak at around 26.3° (2θ) was also observed, indexed to the (0 0 2) plane of the ordered graphitized structure. Kumar et al. has discovered that at elevated temperatures in an oxygen-containing atmosphere, graphite structures oxidize and form graphene oxide (GO), with a peak appearing at around 42.06° (2θ). When temperatures exceed 200 °C, graphene oxide undergoes reduction, causing the shift of peak from 26.3° to 25.8° (2θ). Both can be vaguely observed in AWC-3–800 as well [54].

In all AWC samples, it is evident from their characteristics that various factors such as carbonization temperature, time, activation agent to carbon material ratio, as well as process atmosphere, influence physical and chemical properties. Despite the unique advantages of each sample, AWC-3–700 and AWC-3–800 appear promising candidates, both due to their improved micropore surface area and volume, when it comes to applications that require a high surface area and high adsorption capacity. On the other hand, AWC-2–800 exhibits a higher level of crystallinity, indicating a more stable structure. By contrast, the reference material (YP-80F) does not display the same enhanced properties, which indicates how effective the tailor-made processing conditions were.

Scanning Electron Microscopy (SEM) analysis was conducted using the Helios 5 UX instrument from Thermo Fischer Scientific, USA, to examine the surface morphology of the AWC samples (see Fig. 3). The analysis revealed a wide range of particle sizes, ranging from a few nanometers, predominantly clustered in different configurations around larger particles, to several tens of micrometers. Notably, AWC-3–800 exhibits structures resembling graphene sheets.

2.2. Activated carbon ink fabrication

For the inks utilizing the AC materials, chitosan is used as a binder. To prepare the chitosan solution, 1.7 g of chitosan (Sigma-Aldrich, catalog number 50,494) is dissolved in 67 g of water containing 0.7 g of acetic acid (approximately a 1 % acetic acid solution). The dissolution process is conducted using a magnetic stirrer, which is heated to 50 °C to expedite dissolution. Subsequently, the chitosan solution, totaling approximately 69 g, is transferred into a zip lock bag, to which 20 g of water is added. Next, 30.9 g of AC powder is introduced into the bag, which is then sealed. Mixing of the AC with the chitosan solution is initiated by manually squeezing the bag and utilizing a small roller for approximately 15 min. However, an additional 6.7 g of water is added to the YP-80F AC sample and approximately 14–18 g to the AWC samples to achieve the desired low viscosity and fluidic ink consistency. The manual squeezing and roller manipulation effectively dispersed any

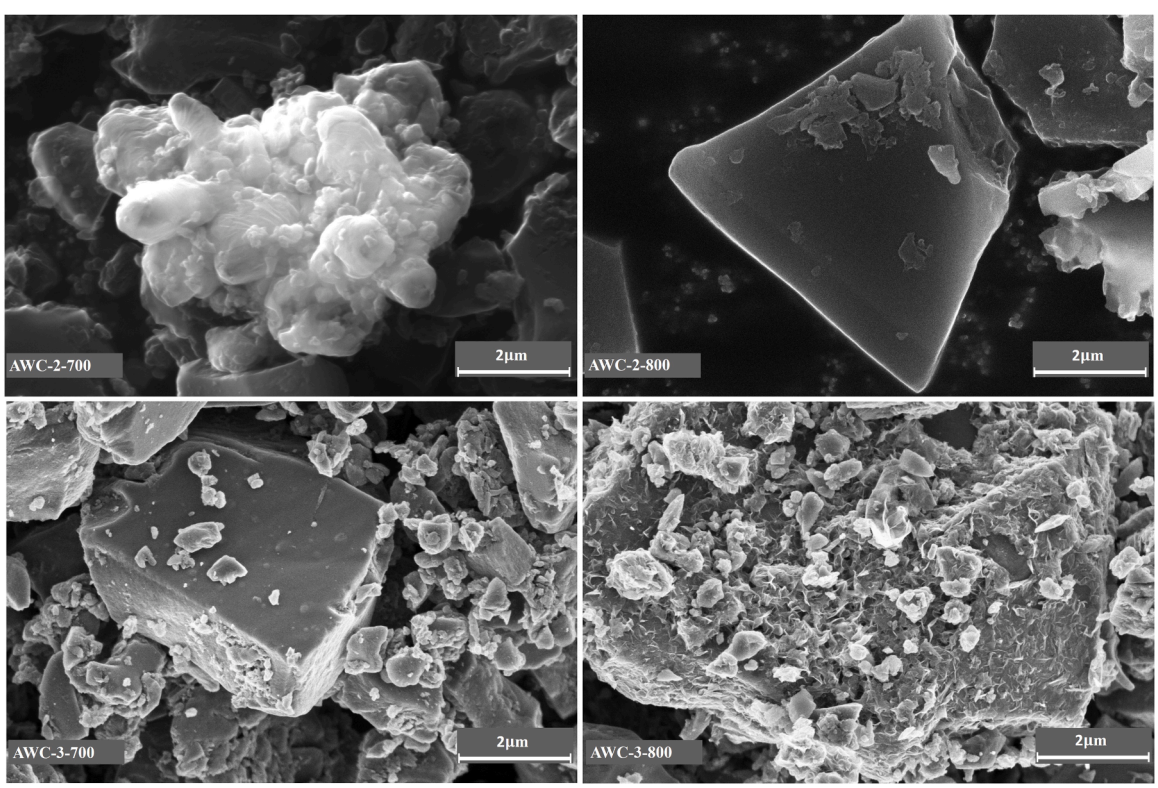

Fig. 3. SEM images of AWC samples.

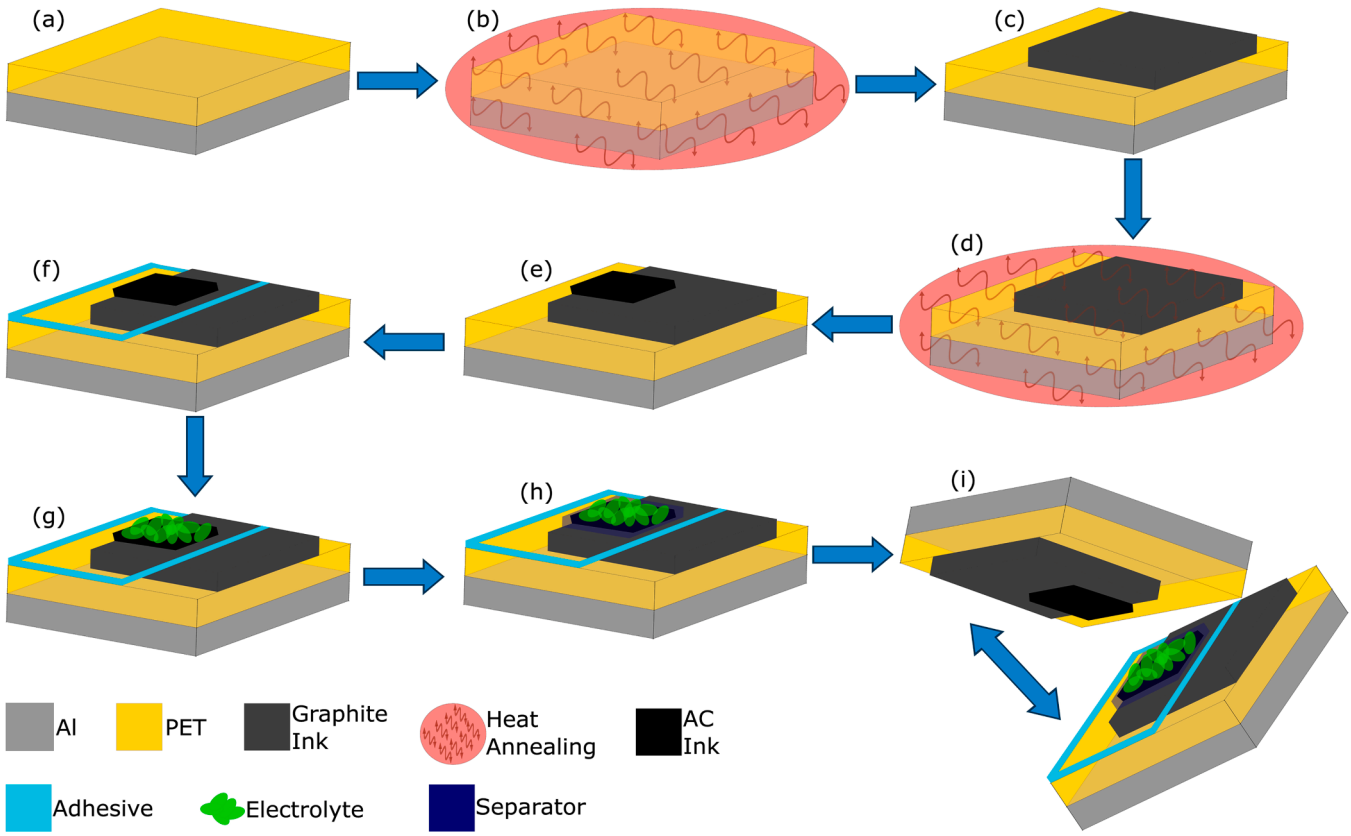

Fig. 4. SC fabrication steps. (a) Al/PET substrate. (b) Pre-heating of the substrate. (c) Deposition of graphite ink on the PET side. (d) Drying of the graphite ink. (e) Deposition of AC ink to form the electrode layer. (f) Application of adhesive onto the PET and part of the current collector layer. (g) Addition of aqueous electrolyte onto the electrode layer. (h) Placement of a cellulose paper separator onto the electrode. (i) Assembly and sealing of the two electrodes face to face.

agglomerates within the mixture.

2.3. Electrolyte preparation

In addition to selection of electrode materials, electrolytes play an important role in determining the overall performance of SCs. Two distinct aqueous electrolytes were used during the fabrication of SCs in order to compare leakage currents and ESRs, as well as to address environmental concerns. Aqueous electrolytes are advantageous due to their high ionic conductivity, low cost, and environmental friendliness [55]. Moreover, they are readily available and compatible with a variety of electrode materials, making them suitable for use in a variety of SC applications.

The first electrolyte comprises a NaCl solution with a mass ratio of 1:5 with water, respectively. As the second electrolyte, a buffer potassium phosphate electrolyte, denoted as $K_xH_yPO_4$, is employed. This electrolyte mixture is formulated by combining 1 M K_2HPO_4 and 1 M KH_2PO_4, adjusted to a pH value of 7 (experimentally measured as 6.93, measured using a Hanna Instruments HI-5521, two-channel research-grade benchtop pH/ORP and EC/TDS/Salinity/Resistivity meter).

2.4. Supercapacitor fabrication

The fabrication process of these printed SCs has been previously documented by the research group [56–59]. However, in this study, some modifications have been introduced to streamline the process. Notably, the use of heat-sealing adhesive has been omitted, eliminating the need for thermal annealing the heat-sealing layer. Instead, the commercially available 3 M 468MP adhesive is employed. This approach also eliminates the requirement for a heat-sealing machine to package the cells.

The fabrication steps are summarized briefly here and depicted schematically in Fig. 4. Initially, as a substrate an Al/PET flexible laminate (Pyroll) is utilized, with an aluminum (Al) thickness of 9 μm and a polyethylene terephthalate (PET) thickness of 50 μm (Fig. 4a). Prior to fabrication, the Al/PET substrate undergoes pre-heating inside an oven at 95 °C for 15 min (Fig. 4b). Subsequently, a current collector layer composed of graphite ink (Acheson Electrodag PF-407C) is applied onto the PET side of the substrate by using a laboratory scale doctor blade coater, with the Al layer serving as a barrier layer (Fig. 4c). The graphite ink is then dried in the oven for 1 hour at 95 °C (Fig. 4d), resulting in a graphite thickness of 25–35 μm. Next, AC ink is applied by using a doctor blade to form an electrode layer on top of the current collector layer (Fig. 4e). The AC ink is left to dry at room temperature overnight, producing a film with a thickness of 30–40 μm. Following this, the 3 M 468MP adhesive is applied onto the PET and part of the current collector layer (Fig. 4f). Subsequently, aqueous electrolyte is added onto the electrode layer (Fig. 4g). The next step involves placing the commercial 40 μm thick Dynacap GT 0.45/40 cellulose paper as the separator onto the electrode, with both the electrode and paper separator being impregnated with aqueous electrolyte (Fig. 4h). Finally, the two electrodes (with identical electrode patterns but facing upside down, one without the paper separator) are assembled and sealed face to face using the sealing adhesive (Fig. 4i). The resulting dimensions of the fabricated SC with the packaging are 50 mm in length, 50 mm in width, and 0.35–0.45 mm in thickness.

2.5. Supercapacitor characterization

The key electrical characteristics of SCs, such as capacitance, ESR, and leakage current, are determined following the guidelines outlined in the international industrial standard IEC 62,391–1 [60]. SCs have been

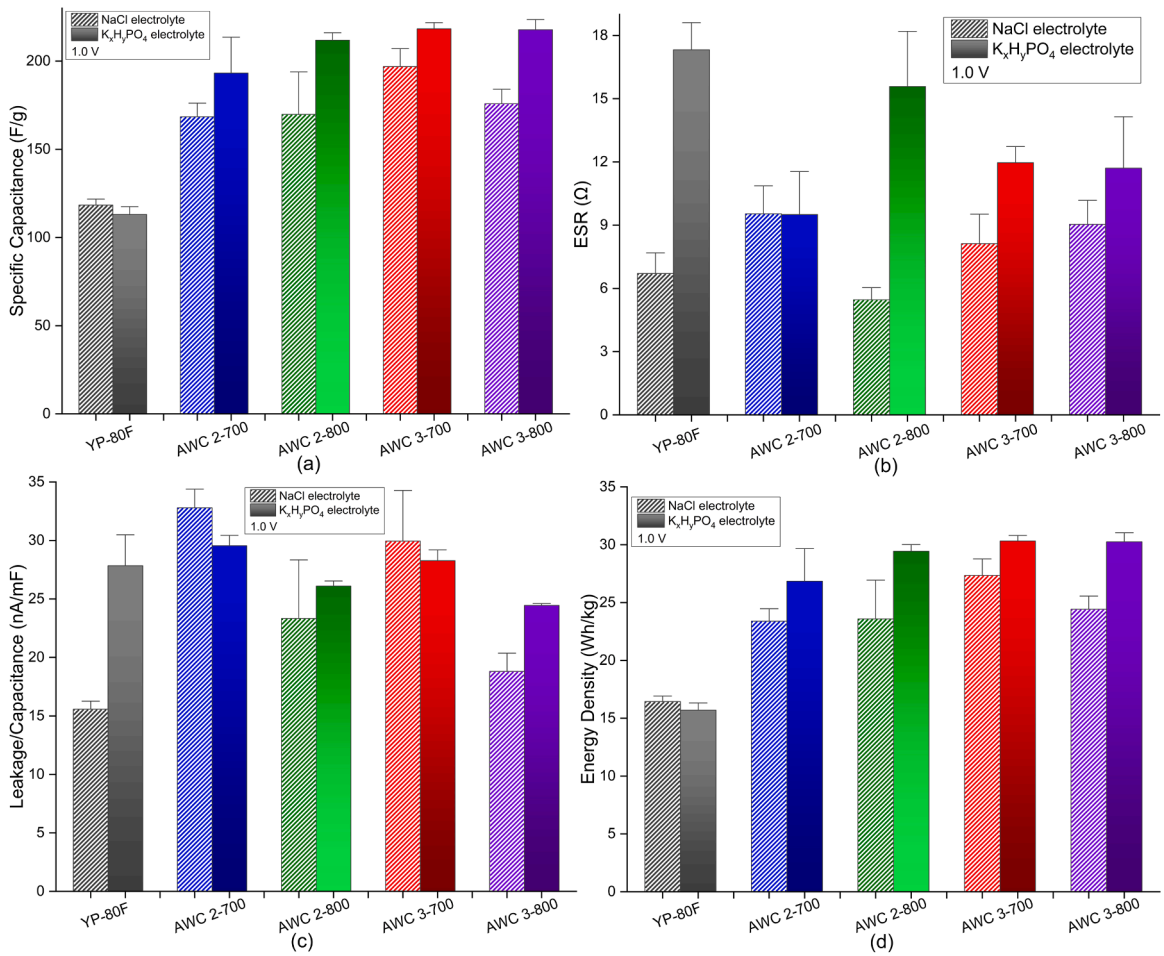

Fig. 5. Average measurements of key parameters for printed SCs characterized at 1.0 V, featuring various electrode and electrolyte materials: (a) specific capacitance of individual electrodes, (b) equivalent series resistance (ESR), (c) leakage per capacitance, and (d) energy density.

characterized with Maccor 4300 workstation (Maccor Inc., USA), undergoing three cycles of charging and discharging within the voltage range of 0 to 1.2 V. Following this, the SCs are stabilized at a constant voltage of 1.2 V for a duration of 30 min. Capacitance is then determined during a discharge step maintaining a constant current between 0.96 V and 0.48 V. Subsequently, the SCs are held at the fixed voltage of 1.2 V for one hour to assess leakage current. The process is repeated for three current levels of 1, 3, and 10 mA. Ultimately, the ESR is computed based on the IR drop observed during the discharge measurement conducted at a current of 10 mA.

3. Results and discussion

In order to facilitate an equitable evaluation between various AWC and commercial reference AC material as well as the electrolytes, four to six printed SCs are fabricated for each category. Subsequently, the mean values of all relevant parameters from the printed SCs are computed and compared. Figs. 5 and 6 display the diverse characterization parameters for each type of fabricated SCs, evaluated at 1.0 V and 1.2 V respectively. The electrochemical potential window limit of the two aqueous electrolytes employed in this study is 1 .2V.

We have also included 90 % confidence intervals (in Figs. 5 and 6) in the bar chart diagrams to ensure the reliability of the results. Confidence intervals tell us where the true mean of the data lies within a range of values. When the confidence level for the calculation is 90 %, then the interval will contain a 90 % probability that the true mean value of the parameter is within that interval. The confidence intervals are used to account for variability and uncertainty in the data, thereby providing a more robust and accurate comparison between the different SC types by taking into account these factors. Using this approach, we can demonstrate the precision and reliability of the measured values, which enhances the credibility of our results.

3.1. Specific capacitance

In order to obtain the specific capacitance of a single electrode (active material on a single electrode) within a printed SC, the specific capacitance of the entire SC, as characterized by the Maccor system, is multiplied by four. This adjustment is made because both electrodes of an SC typically contain approximately equal masses of active material and exhibit symmetry.

As depicted in Figs. 5a and 6a, the specific capacitance of printed SCs crafted with AWC materials surpasses that of SCs utilizing the reference YP-80 AC. This enhancement is noticeable across both types of aqueous electrolytes. Specifically, Fig. 5a demonstrates that the specific capacitance of printed SCs employing AWC materials with $K_xH_yPO_4$ electrolyte, characterized at 1.0 V, exhibits an increase ranging from 71 % (AWC 2–700) to 93 % (AWC 3–700, AWC 3–800) compared to the Kuraray YP-80F AC material. Similarly at 1.0 V characterization, with NaCl as the electrolyte, the specific capacitance demonstrates an increase from 42 % (AWC 2–700) to 67 % (AWC 3–700) relative to the benchmark YP-80F. When characterized at 1.2 V, the specific capacitance of SCs utilizing AWC materials with $K_xH_yPO_4$ electrolyte shows an enhancement of 58 % (AWC 2–700) to 90 % (AWC 3–800) relative to the Kuraray YP-80F as the reference material (Fig. 6a). Additionally, with NaCl electrolyte and characterized at 1.2 V, this increase in specific

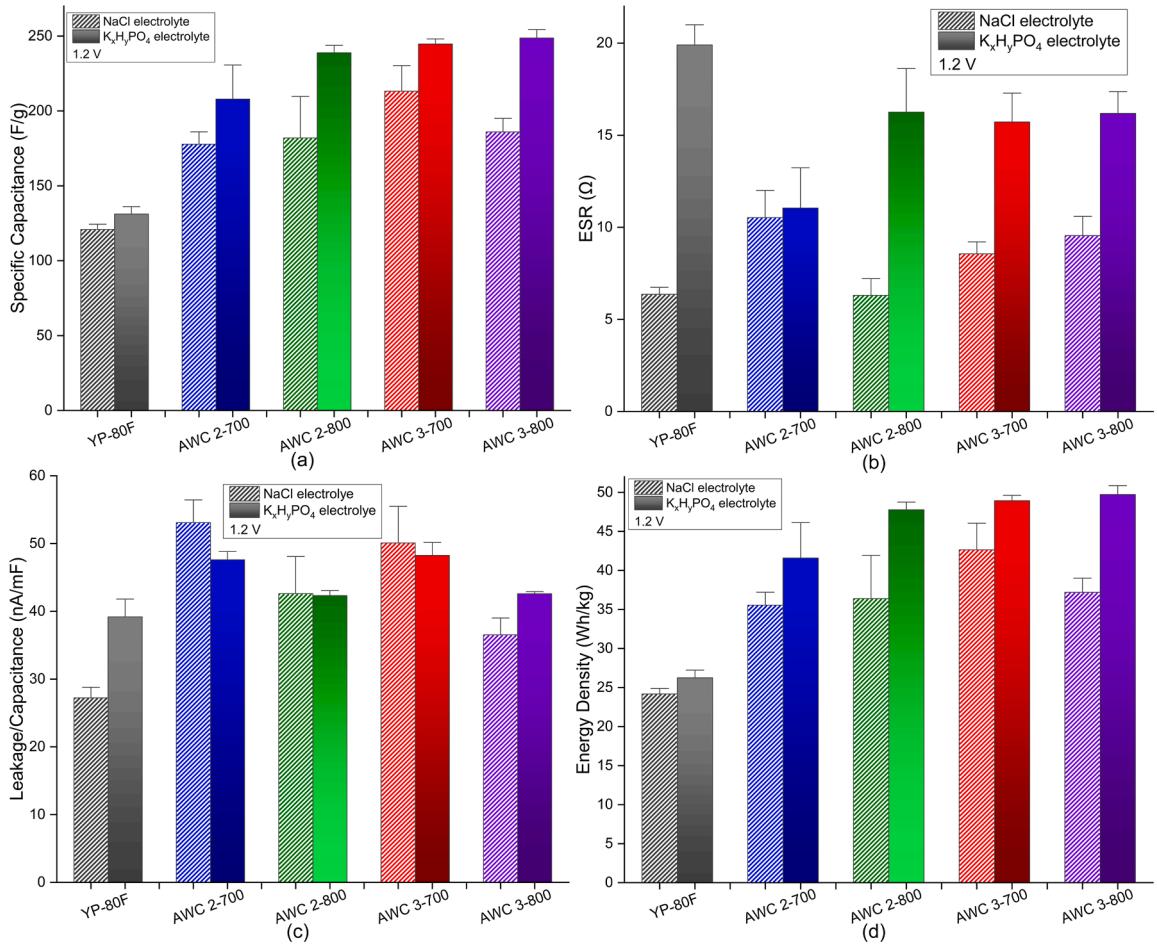

Fig. 6. Average measurements of key parameters for printed SCs characterized at 1.2 V, featuring various electrode and electrolyte materials: (a) specific capacitance, (b) equivalent series resistance (ESR), (c) leakage per capacitance, and (d) energy density.

Table 3
Specific capacitance (F/g) for individual electrodes of printed SCs fabricated using various AC materials and two different types of aqueous electrolytes at characterization voltages of 1.0 V and 1 .2V.

	NaCl		$K_xH_yPO_4$	
	1.0 V	1.2 V	1.0 V	1.2 V
YP-80F	118	121	113	131
AWC 2–700	168	178	193	208
AWC 2–800	170	182	212	239
AWC 3–700	197	213	218	245
AWC 3–800	176	186	218	249

capacitance ranges between 47 % (AWC 2–700) and 76 % (AWC 3–700) compared to YP-80F. Table 3 presents the exact values for the specific capacitance of a singular electrode of the printed SCs manufactured using various AC materials and two types of electrolytes at both 1.0 V and 1.2 V characterization voltages.

In the comprehensive analysis of SCs fabricated using AWC materials, significant increases in specific capacitance were observed, emphasizing the critical role played by porous properties in electrochemical performance. As a result of their enhanced porous characteristics, AWC materials perform better than conventional Kuraray YP-80F AC materials. Due to the increased surface area and volume of pores in AWC materials, ion storage capacity is increased and more active sites for ion adsorption are provided. As a result of these features, printed SCs are capable of achieving higher specific capacitances. The AWC 3–700 and AWC 3–800, which exhibit the greatest increases in specific capacitance, also exhibit a noticeably finer microporosity and a more favorable pore size distribution. As a result of the finer porosity and more advantageous distribution of pore sizes, the ion diffusion kinetics are likely to be enhanced, which is beneficial to the efficient charge-discharge cycles necessary for high-performance SCs. The role of surface chemistry in these observations should also be taken into consideration. The sorptometry measurements indicate improved porous properties, but the surface functional groups and chemical composition of AWC materials may also contribute significantly to the improved electrochemical performance.

Conversely, the higher specific capacitance observed in printed SCs fabricated with $K_xH_yPO_4$ electrolytes compared to those fabricated with NaCl can be attributed to a number of electrochemical and physical factors associated with the electrolytes and their interactions with electrodes. In spite of the fact that potassium ions ($K+$) are larger than sodium ions (Na+), the extent of hydration of Na+ ions is greater than that of $K+$ ions. Consequently, hydrated Na+ ions have a larger effective radius and mass, making them less mobile than $K+$ ions. As $K+$ ions have a higher mobility, they are able to enter the micropores of the AWC more easily, thereby effectively utilizing the electrode's porous structure and increasing the area available for ion adsorption, which is directly proportional to the increase in specific capacitance. Furthermore, the chemical compatibility of $K_xH_yPO_4$ with AWC electrodes also plays a crucial role. In $K_xH_yPO_4$, the phosphate ions may interact more favorably with the carbon surface, which may result in better double-layer formation. In other words, $K_xH_yPO_4$ type SCs have a higher specific capacitance due to a higher pseudocapacitive contribution from faradaic reactions associated with water decomposition and functional surface

groups. It is common to observe higher capacitance values as the SC approaches its maximum voltage. In the case of the phosphate system, this occurs as a result of its high buffer capacity bringing it closer to the stability limit.

These factors combine to explain why SCs using $K_xH_yPO_4$ electrolyte outperform those with NaCl in terms of specific capacitance, highlighting the importance of choosing an appropriate electrolyte to optimize SC performance based on the specific requirements of the application. Moreover, the specific capacitance improvements at different voltages further illustrate the impact of the electrode's porous properties. The results indicate that both the type of electrolyte and the voltage at which the SCs are characterized affect the capacitance, with higher improvements noted at specific combinations of these factors.

Considering the correlation between the porous structure of the AWC materials and their electrochemical capabilities with different electrolytes, it can be concluded that material selection and design are of crucial importance when it comes to developing advanced printed SCs that are integrated with active materials. As a result of these insights into the material properties of the SC, we can optimize the performance of the SC and guide the development of next-generation energy storage systems.

3.2. Equivalent series resistance (ESR)

Regarding the ESR, as illustrated in Fig. 5b and characterized at 1.0 V, all AWC SCs utilizing $K_xH_yPO_4$ electrolyte exhibit a reduction in ESR relative to the Kuraray YP-80F, with the greatest reduction being 45 % (AWC 2–700). Conversely, when NaCl electrolyte is employed, only AWC 2–800 experiences a 19 % decrease in ESR, while the remaining three AWC SCs show an increase in ESR, with the highest increase reaching 42 % (AWC 2–700) compared to the YP-80F SC. The observed trend persists at a characterization voltage of 1.2 V, as depicted in Fig. 6b. All four AWC printed SCs using $K_xH_yPO_4$ electrolyte exhibit a reduction in ESR, with AWC 2–700 showing the largest decrease at 44 % relative to the Kuraray YP-80F SC. Similarly, at 1.2 V, only AWC 2–800 presents a modest ESR reduction, whereas the other three AWC SCs display an increase in ESR, with AWC 2–700 experiencing the most significant rise at 66 % compared to the YP-80F SC.

The observed differences in ESR among the AWC printed SCs can be intricately linked to the porous properties of the AWC materials used. These differences highlight how structural characteristics of the electrodes influence electrochemical performance, particularly under varied electrolytic conditions.

AWC 2–700 showed a significant reduction in ESR when using $K_xH_yPO_4$ electrolyte at both 1.0 V and 1.2 V (45 % and 44 % reduction, respectively), which is attributed to its high pore volume. Due to these properties, the electrolyte is better able to reach the electrode's surface and ion transport dynamics are improved, which results in a lower ESR. Due to the better performance of AWC 2–700, it suggests that its micropore structure best accommodates $K_xH_yPO_4$ ions, which may be more mobile than those in NaCl, resulting in more efficient charge propagation and reduced resistance.

Conversely, when NaCl is used as the electrolyte, most AWC materials except for AWC 2–800 show an increase in ESR, with AWC 2–700 experiencing the most substantial rise (up to 66 % at 1.2 V). This increase in ESR could be largely attributed to experimental variations, such as contact resistance and potential wetting issues. The slight decrease in ESR observed with AWC 2–800 might be attributed to its unique pore size distribution and surface properties, which somehow better accommodate the NaCl ions compared to other AWC samples.

Besides, the observation that printed SCs fabricated using NaCl electrolyte generally exhibit lower ESR compared to those using $K_xH_yPO_4$ for the same SC type can be explained through the higher conductivity of NaCl electrolyte compared to K_xH_yPO4.

Table 4
Energy density (Wh/kg) of printed SCs fabricated using various AC materials and two different types of aqueous electrolytes at characterization voltages of 1.0 V and 1 .2V.

	NaCl		$K_xH_yPO_4$	
	1.0 V	1.2 V	1.0 V	1.2 V
YP-80F	16.4	24.2	15.7	26.2
AWC 2–700	23.4	35.6	26.8	41.6
AWC 2–800	23.6	36.4	29.4	47.8
AWC 3–700	27.4	42.6	30.3	49.0
AWC 3–800	24.4	37.2	30.3	49.8

3.3. Leakage current

In this work, we have adopted leakage current per unit of capacitance as the metric for evaluating leakage current in printed SCs. Using this approach, leakage is measured in nanoamperes per millifarad (nA/mF), which has some advantages. As a result of this, fair comparisons can be made between different SCs regardless of their capacitance sizes since this method is based on a normalized measure. Due to this normalization, it becomes possible to accurately evaluate the efficiency of SCs, where a lower leakage per capacitance indicates a higher energy retention. As well as serving as a performance indicator, this metric also indicates the stability of the SC's performance. The lower the value, the more reliable and stable the SC is under operational conditions, which is essential for practical applications.

According to the data presented in Figs. 5c and 6c, which include SCs characterized at 1.0 V and 1.2 V using both $K_xH_yPO_4$ and NaCl electrolytes, there is generally an increase in leakage per capacitance when using AWC materials for the electrodes compared to the commercial Kuraray YP-80F. However, a notable exception occurs at 1.0 V with $K_xH_yPO_4$ electrolyte, where SCs made with AWC 2–800 and AWC 3–800 exhibit a slight decrease in leakage per capacitance relative to YP-80F. This observation highlights the potential for enhanced efficiency in these specific SCs under selected conditions.

However, the generally observed trend of increased leakage current per capacitance in printed SC using AWC samples can be attributed to the increased amount of functional groups on the surface of AWC materials which can participate in parasitic reactions, resulting in increased leakage currents. While these functional groups may enhance electrochemical reactivity and ion diffusion, they may also lead to undesirable side reactions, leading to leakage currents instead of useful energy storage [61].

In essence, the observed increase in leakage per capacitance in SCs with AWC electrodes is indicative of a complex balance between improving capacitance and managing inefficiencies such as leakage. It is clear from these findings that it is imperative to optimize both the pore structure and surface properties, including the control of functional groups, not only to maximize capacitance but also to control and reduce leakage currents in order to produce more efficient energy storage devices.

3.4. Energy density

With respect to energy density, we report the energy density of the SC's single electrode in Wh/kg, calculated using the formula $(C_s \times V^2) / (2 \times 3.6)$, where '$C_s$' represents the specific capacitance values from Table 3, and 'V' is the characterization voltage.

Figs. 5d and 6d illustrate that printed SCs utilizing AWC materials generally exhibit an increase in energy density compared to those using commercial Kuraray YP-80F, across both characterized voltages (1.0 V and 1.2 V) and electrolyte types. Specifically, at 1.0 V, in case of NaCl electrolyte, the AWC-3–700 SC shows an energy density of 27.4 Wh/kg, which is 67 % higher than that of the YP-80F. When using the K_xH_yPO4 electrolyte, the AWC-3–700 and AWC-3–800 SCs report energy densities

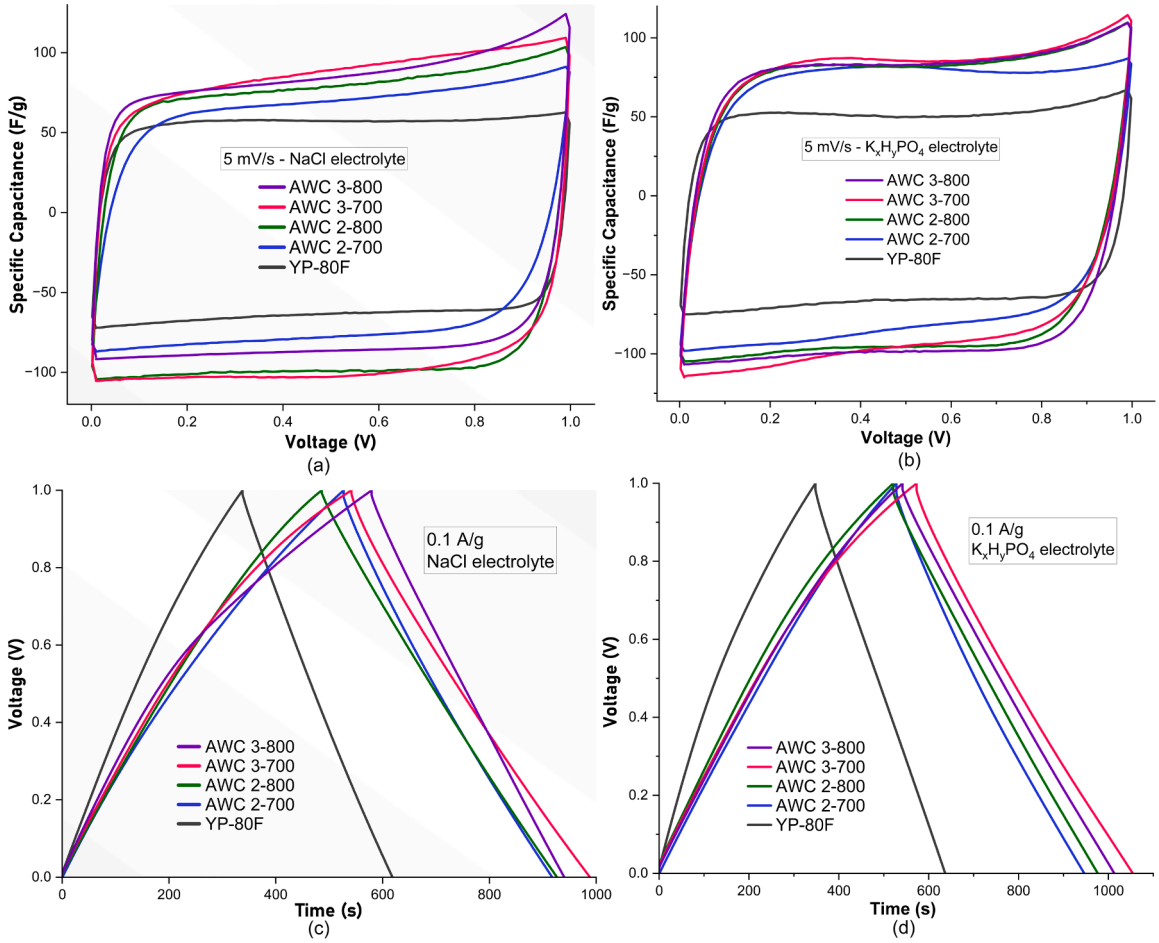

Fig. 7. CV curves (scan rate of 5 mV/s) and GCD curves (0.1 A/g) of printed SCs incorporating various AWC materials and reference YP-80F, utilizing NaCl and K_xH_yPO4 electrolytes, characterized at 1.0 V. (a) CV curves of NaCl electrolyte SCs. (b) CV curves of K_xH_yPO4 electrolyte SCs. (c) GCD curves of NaCl electrolyte SCs. (d) GCD curves of K_xH_yPO4 electrolyte SCs.

of 30.3 Wh/kg at 1.0 V, marking approximately a 93 % increase over the YP-80F model. At a characterization voltage of 1.2 V with the NaCl electrolyte, the AWC 3–700 SC presents an energy density of 42.6 Wh/kg, achieving an 76 % increase compared to the YP-80F. With the K_xH_yPO4 electrolyte at the same voltage, the AWC-3–800 SC demonstrate energy density of 49.8 Wh/kg, which is 90 % increase over the YP-80F, indicating significant improvement in energy storage capability. Table 4 displays the precise energy density values of the printed SCs produced with the AWC materials and reference YP-80F utilizing both NaCl and $K_xH_yPO_4$ electrolyte, at characterization voltages of 1.0 V and 1.2 V.

The observed trends in energy density in printed SCs utilizing AWC materials across various characterization conditions reveal insightful correlations with the sorptometry data that highlight the role of electrode material properties and electrolyte type on performance. The increases in energy density across AWC samples in comparison to the commercial Kuraray YP-80F across different voltages and electrolyte types illustrate the beneficial effects of the AWC materials' extensive surface area and pore volume. These structural characteristics enhance the SCs' ability to store more electrolyte ions and facilitate easier ion transport, directly boosting capacitance and energy storage capacity.

On the other hand, generally, across similar types of AWC materials used as electrodes in printed SCs, those utilizing $K_xH_yPO_4$ electrolyte consistently exhibit higher energy densities than those with NaCl electrolyte at both 1.0 V and 1.2 V characterizations (Figs. 5d, 6d and Table 4). In contrast, for SCs made with the reference Kuraray YP-80F AC material, the energy densities remain relatively similar across both electrolytes at the same voltages.

The performance differences in printed SCs using AWC materials with various electrolytes are closely linked to the unique sorptometric characteristics of the electrode materials. The observed higher energy densities in SCs with the $K_xH_yPO_4$ electrolyte suggest that the microporosity and surface areas of the AWC materials are optimally aligned with the molecular structure and ion mobility of $K_xH_yPO_4$, thereby enhancing ion storage capacity and energy density.

The consistent energy densities observed in SCs made with Kuraray YP-80F AC material across both electrolytes illustrate the importance of electrolyte-electrode interaction dynamics. YP-80F is likely to perform consistently across a wide range of electrolytes due to its unique chemistry and porous structure. There may be a good balance between the pore size distribution, the surface functional groups, and the electrochemical stability of YP-80F, which may allow it to make effective use of NaCl electrolyte despite its potential limitations when compared with $K_xH_yPO_4$. Additionally, YP-80F may exhibit consistent performance due to the presence of fewer functional groups, which may make it less sensitive to reactions involving the electrolyte solution. Hence, when designing high-performance SCs, consideration should be given not only to the intrinsic properties of carbon materials but also to their compatibility with different electrolytes. Accordingly, to maximize the efficiency and functionality of SCs in various applications, electrolytes should be tailored to the specific structural and chemical properties of electrode materials.

These findings demonstrate the importance of maintaining an ideal balance between maximizing ion storage capabilities and maintaining

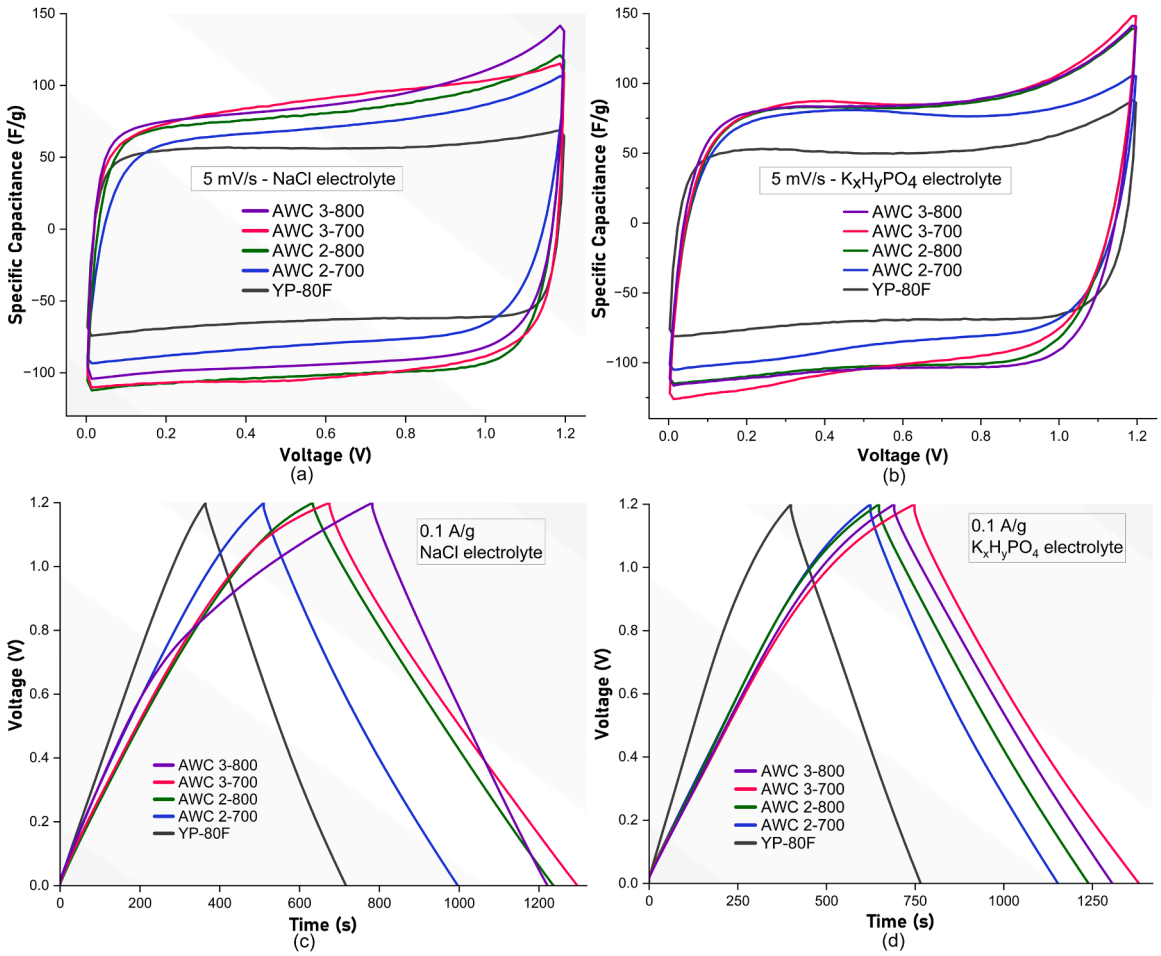

Fig. 8. CV curves (scan rate of 5 mV/s) and GCD curves (0.1 A/g) of printed SCs incorporating various AWC materials and reference YP-80F, utilizing NaCl and K_xH_yPO4 electrolytes, characterized at 1.2 V. (a) CV curves of NaCl electrolyte SCs. (b) CV curves of K_xH_yPO4 electrolyte SCs. (c) GCD curves of NaCl electrolyte SCs. (d) GCD curves of K_xH_yPO4 electrolyte SCs.

efficient ion mobility in order to maximize the performance of SCs. The AWC materials' pore structure appears exceptionally well-suited to enhancing energy storage by maximizing ion accommodation. This analysis emphasizes the importance of matching electrode material properties with specific electrolyte characteristics to achieve the desired energy storage capacities in SC applications, promoting a targeted approach in material and electrolyte selection to meet specific performance requirements.

3.5. CV and gcd measurements

The cyclic voltammetry (CV) and galvanostatic charge-discharge (GCD) analyses of the printed SCs (one sample per each type) incorporating AWC and reference YP-80F materials, employing NaCl and $K_xH_yPO_4$ electrolytes, are illustrated in Figs. 7 and 8, respectively at characterization voltages of 1.0 V and 1.2 V. CV measurements were conducted at a scan rate of 5 mV/s, while GCD measurements were performed at a current density of 0.1 A/g. Utilizing current density, measured in amperes per gram, ensures scalability and facilitates comparability by standardizing the results to the mass of the active material. This approach allows for direct comparisons irrespective of the amount of material utilized. Current density emphasizes the efficiency of the electrode material, illustrating its ability to store and discharge charge effectively per unit mass.

As depicted in Figs. 7a, 7b, 8a, and 8b, the CV curves affirm that AWC SCs exhibit superior specific capacitance compared to the reference YP-80F for both electrolyte types and characterization voltages. In addition, AWC 3–700 and AWC 3–800 SCs exhibit superior performance in CV curves for both electrolyte types and at both characterization voltages, demonstrating higher specific capacitance and energy density.

Regarding the GCD results, as illustrated in Figs. 7c, 7d, 8c, and 8d, it is evident for both electrolytes and at both characterization voltages that AWC-type SCs exhibit broader GCD curves (prolonged charge/discharge durations) compared to the reference YP-80F one, indicating higher specific capacitance and the ability to retain charge for extended periods before complete discharge. Furthermore, the superior performance of AWC 3–700 and AWC 3–800 SCs is evident in the GCD curves for both electrolyte types and at both voltages.

It should be noted, however, that a detailed examination of the GCD curves also confirms that AWC 3–800 type SC has certain limitations in terms of performance. In particular, as shown in Figs. 7c and 8c, AWC 3–800 exhibits deviations from ideal capacitive behavior, manifested in less perfectly curved profiles and signs of irreversibility. There may be parasitic reactions occurring, likely due to the decomposition of the electrolyte, water, or surface functional groups, particularly at higher voltages. Irreversibility indicates that there are significant chemical reactions occurring within the system, affecting the charge-discharge process.

In order to optimize the performance and durability of SCs, these issues must be addressed. Future research should focus on improving the stability of electrode materials and improving the compatibility of electrolytes in order to mitigate unwanted reactions and increase overall performance and reliability.

4. Summary and conclusion

This study provides novel insights into the role of biomass-derived Activated Wood Carbon (AWC) in energy storage applications, particularly in advancing printed supercapacitors (SCs) with sustainable and environmentally friendly materials. Through comprehensive analyses, including sorptometry, Raman spectroscopy, XRD, and electrochemical assessments, we identified the key structural and electrochemical factors influencing SC performance.

The findings demonstrate that printed SCs utilizing AWC significantly outperform those fabricated with conventional Kuraray YP-80F activated carbon. Specifically, AWC-based SCs achieved up to 93 % higher specific capacitance and 90 % higher energy density at operating voltages of 1.0 V and 1.2 V, respectively. These enhancements are attributed to AWC's superior surface area and pore volume, which facilitate increased ion storage and improved ion mobility—critical factors for high-performance SCs.

Electrolyte type also plays a crucial role in SC performance. Devices utilizing the $K_xH_yPO_4$ electrolyte exhibited higher specific capacitance and energy density compared to those with NaCl, primarily due to increased pseudocapacitive contributions from faradaic reactions involving water decomposition and functional surface groups. This highlights the synergy between AWC's porous structure and its compatibility with optimized electrolytes.

The results further underline the potential of biomass-derived carbon materials to create high-performing SCs that align with global sustainability objectives by reducing reliance on non-renewable resources. By optimizing the processing techniques, surface properties, and electrolyte configurations, future studies can unlock additional performance improvements. These efforts will enable the development of next-generation energy storage technologies that are both efficient and sustainable.

CRediT authorship contribution statement

Hamed Pourkheirollah: Conceptualization, Data curation, Formal analysis, Investigation, Methodology, Software, Visualization, Writing – original draft, Writing – review & editing. **Remuel Isaac M. Vitto:** Conceptualization, Data curation, Methodology, Software, Visualization, Writing – review & editing. **Aleksandrs Volperts:** Data curation, Investigation, Resources, Supervision, Writing – original draft, Writing – review & editing. **Steffen Thrane Vindt:** Data curation, Investigation, Methodology, Supervision, Writing – review & editing. **Līga Grīnberga:** Conceptualization, Resources, Writing – original draft, Writing – review & editing. **Gints Kučinskis:** Formal analysis, Methodology, Resources, Supervision, Writing – review & editing. **Jari Keskinen:** Data curation, Formal analysis, Investigation, Methodology, Supervision, Writing – review & editing. **Matti Mäntysalo:** Formal analysis, Funding acquisition, Project administration, Resources, Supervision, Writing – review & editing.

Declaration of competing interest

The authors declare that they have no known competing financial interests or personal relationships that could have appeared to influence the work reported in this paper.

Acknowledgements

This project, funded by the European Commission's Horizon Europe programme, is part of the Graphene Flagship initiative which works to advance technologies that rely on graphene and other 2D materials. Part of the research uses Academy of Finland Research Infrastructure 'Printed Intelligence Infrastructure' (PII-FIRI, Grant Number 358618). SEM images were obtained by Ph.D. Guna Krieķe at the Insitute of Solid State Physics, University of Latvia that has received funding from the European Union's Horizon 2020 Framework Programme H2020-WIDESPREAD-01–2016–2017-TeamingPhase2 under grant agreement No 739508, project CAMART[2].

Data availability

Data will be made available on request.

References

[1] R. Wolniak, Boż Skotnicka-Zasadzień, Development of photovoltaic energy in EU countries as an alternative to fossil fuels, Energies 15 (2) (2022) 662.
[2] A. Blakers, M. Stocks, B. Lu, C. Cheng, A review of pumped hydro energy storage, Progress in Energy 3 (2) (2021) 022003.
[3] A.S. Darwish, R. Al-Dabbagh, Wind energy state of the art: present and future technology advancements, Renew. Energy Environ. Sustain. 5 (2020) 7.
[4] MdN Hussain, MdA Halim, MdYA Khan, S. Ibrahim, A. Haque, A comprehensive review on techniques and challenges of energy harvesting from distributed renewable energy sources for wireless sensor networks, Control Systems and Optimization Letters 2 (1) (2024) 15–22.
[5] A. Kalair, N. Abas, M. Shoaib Saleem, A.R. Kalair, N. Khan, Role of energy storage systems in energy transition from fossil fuels to renewables, Energy Stor. 3 (1) (2021) e135.
[6] A. Khodabandehlo, A. Noori, MS. Rahmanifar, MF. El-Kady, RB. Kaner, MF. Mousavi, Laser-scribed graphene–polyaniline microsupercapacitor for internet-of-things applications, Adv. Funct. Mater. 32 (39) (2022) 2204555.
[7] S. Naeem, A. Ali, K. Memon, M. Bavluwala, U.P. Shinde, A.V. Patil, A review of flexible high-performance supercapacitors for the internet of things (IoT) and artificial intelligence (ai) applications, Energy and Thermofluids Eng. 3 (2023) 1–9.
[8] K. Keum, J.W. Kim, S.Y. Hong, J. Gon Son, S.-S. Lee, J.S. Ha, Flexible/stretchable supercapacitors with novel functionality for wearable electronics, Adv. Mater. 32 (51) (2020) 2002180.
[9] S. Mohsen, A. Zekry, K. Youssef, M. Abouelatta, A self-powered wearable wireless sensor system powered by a hybrid energy harvester for healthcare applications, Wireless Personal Communicat. 116 (4) (2021) 3143–3164.
[10] SY. Attia, SG. Mohamed, YF. Barakat, HH. Hassan, WAl Zoubi, Supercapacitor electrode materials: addressing challenges in mechanism and charge storage, Rev. Inorg. Chem. 42 (1) (2022) 53–88.
[11] M. Hepel, Advances in micro-supercapacitors (MSCs) with high energy density and fast charge-discharge capabilities for flexible bioelectronic devices—A review, Electrochem. Sci. Adv. 3 (3) (2023) e2100222.
[12] J. Zhao, AF. Burke, Review on supercapacitors: technologies and performance evaluation, J. Energy Chem. 59 (2021) 276–291.
[13] W. Dong, M. Xie, S. Zhao, Q. Qiuliang, H. Fuqiang, Materials design and preparation for high energy density and high power density electrochemical supercapacitors, Mater. Sci. Eng.: R: Reports 152 (2023) 100713.
[14] A.G. Olabi, Q. Abbas, AAl Makky, M.A. Abdelkareem, Supercapacitors as next generation energy storage devices: properties and applications, Energy 248 (2022) 123617.
[15] P. Sharma, V. Kumar, Current technology of supercapacitors: a review, J. Electron. Mater. 49 (6) (2020) 3520–3532.
[16] N. Wu, X. Bai, D. Pan, B. Dong, R. Wei, N. Naik, R. Rangrao Patil, Z. Guo, Recent advances of asymmetric supercapacitors, Adv. Mater. Interf. 8 (1) (2021) 2001710.
[17] J. Huang, S. Han, J. Zhu, Q. Wu, H. Chen, A. Chen, J. Zhang, B. Huang, X. Yang, L. Guan, Mechanically stable all flexible supercapacitors with fracture and fatigue resistance under harsh temperatures, Adv. Funct. Mater. 32 (35) (2022) 2205708.
[18] A. Dutta, S. Mitra, M. Basak, T. Banerjee, A comprehensive review on batteries and supercapacitors: development and challenges since their inception, Energy Storage 5 (1) (2023) e339.
[19] J. Libich, J. Máca, J. Vondrák, O. Čech, M. Sedlaříková, Supercapacitors: properties and applications, J. Energy Storage 17 (2018) 224–227.
[20] M. Chafiq, A. Chaouiki, Y.G. Ko, Advances in COFs for energy storage devices: harnessing the potential of covalent organic framework materials, Energy Storage Materials (2023) 103014.
[21] P. Forouzandeh, V. Kumaravel, SC. Pillai, Electrode materials for supercapacitors: a review of recent advances, Catalysts 10 (9) (2020) 969.
[22] P. Manasa, S. Sambasivam, F. Ran, Recent progress on biomass waste derived activated carbon electrode materials for supercapacitors applications—A review, J. Energy Storage 54 (2022) 105290.
[23] J. Artigas-Arnaudas, BK. Muñoz, M. Sánchez, J. Prado, M. Victoria Utrilla, A. Ureña, Surface modifications of carbon fiber electrodes for structural supercapacitors, Appl. Compos. Mater. (2022) 1–12.
[24] S.W. Bokhari, A.H. Siddique, PC. Sherrell, X. Yue, K.M. Karumbaiah, S. Wei, AV. Ellis, W. Gao, Advances in graphene-based supercapacitor electrodes, Energy Reports 6 (2020) 2768–2784.
[25] B. De, S. Banerjee, K.D. Verma, T. Pal, P.K. Manna, KK. Kar, Carbon nanotube as electrode materials for supercapacitors, Handbook of Nanocomposite Supercapacitor Materials II: Performance (2020) 229–243.
[26] Y. Wang, L. Zhang, H. Hou, W. Xu, G. Duan, S. He, K. Liu, S. Jiang, Recent progress in carbon-based materials for supercapacitor electrodes: a review, J. Mater. Sci. 56 (2021) 173–200.
[27] C. Zhang, H. Wang, Y. Gao, C. Wan, Cellulose-derived carbon aerogels: a novel porous platform for supercapacitor electrodes, Mater. Des. 219 (2022) 110778.

[28] P. Sinha, S. Banerjee, KK. Kar, Activated carbon as electrode materials for supercapacitors, Handbook of Nanocom (posite Supercapacitor Materials II: Performance) (2020) 113–144.
[29] A.T. Adeleye, A.A. Akande, C.K. Odoh, M. Philip, T.T. Fidelis, P.I. Amos, O. O. Banjoko, Efficient synthesis of bio-based activated carbon (AC) for catalytic systems: a green and sustainable approach, J. Ind. Eng. Chem. 96 (2021) 59–75.
[30] A. Adan-Mas, L. Alcaraz, P. Arévalo-Cid, FA. López-Gómez, F. Montemor, Coffee-derived activated carbon from second biowaste for supercapacitor applications, Waste Manage. (Oxford) 120 (2021) 280–289.
[31] B. Shaku, T.P. Mofokeng, N.J. Coville, K.I. Ozoemena, M.S. Maubane-Nkadimeng, Biomass valorisation of marula nutshell waste into nitrogen-doped activated carbon for use in high performance supercapacitors, Electrochim. Acta 442 (2023) 141828.
[32] T.,.D. Japhet, KO. Oyedotun, N.F. Sylla, A.A. Mirghni, N.M. Ndiaye, N. Manyala, Waste chicken bone-derived porous carbon materials as high performance electrode for supercapacitor applications, J. Energy Storage 51 (2022) 104378.
[33] Y. Chen, R. Hu, J. Qi, Y. Sui, Y. He, Q. Meng, F. Wei, Y. Ren, Sustainable synthesis of N/S-doped porous carbon sheets derived from waste newspaper for high-performance asymmetric supercapacitor, Mater. Res. Express 6 (9) (2019) 095605.
[34] Yu Ma, J. Yin, H. Liang, D. Yao, Y. Xia, K. Zuo, Yu-P Zeng, A two step approach for making super capacitors from waste wood, J. Clean. Prod. 279 (2021) 123786.
[35] M. Jayachandran, S. Kishore Babu, T. Maiyalagan, N. Rajadurai, T. Vijayakumar, Activated carbon derived from bamboo-leaf with effect of various aqueous electrolytes as electrode material for supercapacitor applications, Mater. Lett. 301 (2021) 130335.
[36] D. Gao, P. Zhao, J. Liu, Y. Zhou, B. Lyu, J. Ma, L. Shao, Polyaniline/silver nanowire cotton fiber: a flexible electrode material for supercapacitor, Adv. Powder Technol. 32 (11) (2021) 3954–3963.
[37] S. Sarkar, A. Arya, U. Kr Gaur, A. Gaur, Investigations on porous carbon derived from sugarcane bagasse as an electrode material for supercapacitors, Biomass Bioenergy 142 (2020) 105730.
[38] C. Qin, S. Wang, Z. Wang, K. Ji, S. Wang, X. Zeng, X. Jiang, G. Liu, Hierarchical porous carbon derived from Gardenia jasminoides Ellis flowers for high performance supercapacitor, J. Energy Storage 33 (2021) 102061.
[39] M. Yeleuov, C. Seidl, T. Temirgaliyeva, A. Taurbekov, N. Prikhodko, B. Lesbayev, F. Sultanov, C. Daulbayev, S. Kumekov, Modified activated graphene-based carbon electrodes from rice husk for supercapacitor applications, Energies 13 (18) (2020) 4943.
[40] R. Ortiz-Olivares, D. David, D.M. Ramón Lobato-Peralta, JA. Arias, A. Okolie, K. Cuentas-Gallegos, P.J. Sebastian, A.R. Mayer, PU. Okoye, Production of nanoarchitectonics corncob activated carbon as electrode material for enhanced supercapacitor performance, J. Energy Storage 55 (2022) 105447.
[41] P. Zhang, W. Wang, Z. Kou, Bo Wang, X. Zhong, Low-cost and advanced symmetry supercapacitors based on three-dimensional tea waste of porous carbon nanosheets, Mater. Technol. 36 (1) (2021) 1–10.
[42] Z. Pan, J. Yang, J. Kong, X.J. Loh, J. Wang, Z. Liu, Porous and Yet Dense" electrodes for high-volumetric-performance electrochemical capacitors: principles, advances, and challenges, Adv. Sci. 9 (4) (2022) 2103953.
[43] S. Wei, C. Wan, Y. Wu, Recent advances in wood-based electrode materials for supercapacitors, Green Chem. 25 (9) (2023) 3322–3353.
[44] Y. Han, M.S. Yang, S.- Lee, Investigation on the awareness and preference for wood culture to promote the values of wood: III. Living environment and trend of wood utilization, J. Korean Wood Sci. Technol. 50 (6) (2022) 375–391.
[45] J. Xu, J. Lei, N. Ming, C. Zhang, K. Huo, Rational design of wood-structured thick electrode for electrochemical energy storage, Adv. Funct. Mater. 32 (35) (2022) 2204426.
[46] H.A. Hamouda, H.I. Abdu, Q. Hu, M.A. Abubaker, H. Lei, S. Cui, AI. Alduma, H. Peng, G. Ma, Z. Lei, Three-dimensional nanoporous activated carbon electrode derived from acacia wood for high-performance supercapacitor, Front Chem 10 (2022) 1024047.
[47] A.R. Selvaraj, D. Chinnadurai, I. Cho, J.-S. Bak, K. Prabakar, Bio-waste wood-derived porous activated carbon with tuned microporosity for high performance supercapacitors, J. Energy Storage 52 (2022) 104928.
[48] Atika, R.K. Dutta, Oxygen-rich porous activated carbon from eucalyptus wood as an efficient supercapacitor electrode, Energy Technol. 9 (9) (2021) 2100463.
[49] Y. Chen, Y. Yu, X. Zhang, C. Guo, C. Chen, S. Wang, D. Min, High performance supercapacitors assembled with hierarchical porous carbonized wood electrode prepared through self-activation, Ind. Crops Prod. 181 (2022) 114802.
[50] A. Jain, M. Ghosh, M. Krajewski, S. Kurungot, M. Michalska, Biomass-derived activated carbon material from native European deciduous trees as an inexpensive and sustainable energy material for supercapacitor application, J. Energy Storage 34 (2021) 102178.
[51] ST. Vindt, EM. Skou, The buffer effect in neutral electrolyte supercapacitors, Appl. Phys. A 122 (2) (2016) 64.
[52] JH. Williams, M. Gbadomosi, AB. Greytak, ML. Myrick, Measuring the surface area of carbon black using BET isotherms: an experiment in physical chemistry, J. Chem. Educ. 100 (12) (2023) 4838–4844.
[53] T.A. Centeno, F. Stoeckli, The assessment of surface areas in porous carbons by two model-independent techniques, the DR equation and DFT, Carbon N Y 48 (9) (2010) 2478–2486.
[54] P. Kumar, N. Divya, J. Kumar Ratan, Study on the physico-chemical properties of reduced graphene oxide with different degrees of reduction temperature, J. Iran. Chem. Soc. 18 (2021) 201–211.
[55] M. Sajjad, M. Ibrar Khan, F. Cheng, W. Lu, A review on selection criteria of aqueous electrolytes performance evaluation for advanced asymmetric supercapacitors, J. Energy Storage 40 (2021) 102729.
[56] H. Pourkheirollah, J. Keskinen, M. Mäntysalo, D. Lupo, An improved exponential model for charge and discharge behavior of printed supercapacitor modules under varying load conditions, J. Power Sources 535 (2022) 231475.
[57] J. Keskinen, S. Lehtimäki, A. Dastpak, S. Tuukkanen, T. Flyktman, T. Kraft, A. Railanmaa, D. Lupo, Architectural modifications for flexible supercapacitor performance optimization, Electron. Mater. Lett. 12 (2016) 795–803.
[58] A. Railanmaa, S. Lehtimäki, J. Keskinen, D. Lupo, Non-toxic printed supercapacitors operating in sub-zero conditions, Sci. Rep. 9 (1) (2019) 14059.
[59] A. Railanmaa, A. Soltani, S. Lehtimäki, N. Pournoori, J. Keskinen, M. Hokka, D. Lupo, Skin-conformable printed supercapacitors and their performance in wear, Sci. Rep. 10 (1) (2020) 15194.
[60] B.B. Standard, Fixed electric double layer capacitors for use in electronic equipment. Part I: generic specification, BS EN (2006), 62391-1.
[61] R. Yuan, Y. Dong, R. Hou, Su Zhang, H. Song, Influencing factors and suppressing strategies of the self-discharge for carbon electrode materials in supercapacitors, J. Electrochem. Soc. 169 (3) (2022) 030504.